Du R et al. (2023) DETERMINING 3D IMAGE STRUCTURES IN ADOLESCENT MYOPIA WITH DEEP LEARNING: IMPACT OF FITNESS AND GAMES. Revista Internacional de Medicina y Ciencias de la Actividad Física y el Deporte vol. 23 (93) pp. 399-415.
DOI: https://doi.org/10.15366/rimcafd2023.93.026

ORIGINAL

DETERMINING 3D IMAGE STRUCTURES IN ADOLESCENT MYOPIA WITH DEEP LEARNING: IMPACT OF FITNESS AND GAMES

Ying Zhi[1], Rui Du[1,*], Ying Qiao[1], Kexin Sang[1], Lili Chen[1], Min Cai[1] and Peiling You[1]

[1] Ophthalmology, Xi'an First Hospital, Xi'an 710002，Shaanxi, China.
E-mail: vdurui@163.com

Recibido 21 de agosto de 2022 **Received** August 21, 2022
Aceptado 26 de octubre de 2023 **Accepted** October 26, 2023

ABSTRACT

In recent years, there has been a notable increase in myopia and refractive issues among adolescents, a trend that is concerning given the importance of visual health in overall well-being and physical activity. This study leverages Artificial Intelligence (AI) and 3D Optical Coherence Tomography Images, utilizing deep learning techniques, to analyze the refractive three-dimensional image structure of adolescent myopia. The aim is to understand how myopia and vision clarity might affect adolescents' engagement in physical fitness and games. An experimental group and a control group were established for this purpose. The analysis of the 3D image structure was conducted using sample analysis methods and fuzzy variable similarity measurement techniques. The results indicated significant variations in stereo vision and anisotropy levels among participants. In the low-level isokinetic inspection group, 34.62% had abnormal findings, while 65.38% were normal. The high anisotropy group showed 60.62% with abnormal results. Notably, in the low anisotropy group, 80.77% had normal stereo vision, but 19.23% were abnormal, with an average stereo vision of 71.92±73.92". The high anisotropy group had more acute stereo vision, with 54.55% normal and 45.45% abnormal cases, and an average stereo vision of 130.91±119.83". The findings demonstrate the effectiveness of the applied 3D image processing methods in analyzing the refractive status of adolescents. Importantly, this analysis is crucial for understanding the impact of myopia on adolescents' ability to engage in physical activities and games, which are essential for their overall physical and mental development. The study highlights the need for further research into how visual impairments affect adolescent participation in physical fitness and games, aiming to improve their

quality of life and health outcomes.

KEYWORDS: artificial intelligence, electronic health, refractive myopia, three-dimensional image structure.

1. INTRODUCTION

Myopia, commonly known as nearsightedness, has become increasingly prevalent among adolescents, posing a significant public health concern. This refractive error impairs distant vision, which can profoundly affect an individual's quality of life, particularly in their formative years(Lu et al., 2021). Recent advancements in Artificial Intelligence (AI), especially in deep learning, have opened new avenues for understanding and managing myopia more effectively. This study focuses on utilizing AI-based 3D Optical Coherence Tomography Images to analyze the refractive three-dimensional image structure of adolescent myopia (Abdalla, Elawamry, Nada, & Helal, 2020; Todorov, Mitrev, & Penev, 2020).

The rise in myopia rates among young people has been paralleled by an increase in sedentary lifestyles and a decrease in outdoor activities. Physical fitness and participation in games are crucial for the overall development of adolescents, impacting their physical health, social skills, mental well-being, and academic performance(Abdalla, Elawamry, Nada, & Helal, 2020; Todorov, Mitrev, & Penev, 2020). However, the visual challenges posed by myopia can deter active participation in these activities. Accurate visual perception is essential in sports and physical games, where depth perception, hand-eye coordination, and spatial awareness play significant roles(Huang, Chang, & Wu, 2015; Karsai, Montano, & Schmickl, 2016; Lanca et al., 2022; Li et al., 2015; Muralidharan et al., 2021).

Given this context, our study aims to determine and analyze various elements of refractive three-dimensional image structures in adolescents with myopia, leveraging deep learning algorithms. This approach aims to provide a more nuanced understanding of how myopia affects visual function in dynamic environments, like those encountered during physical activities and games (Ang et al., 2019). The study's design includes an experimental group and a control group, employing sample analysis methods and fuzzy variable similarity measurement methods to analyze the data(Pitts, 2020).

Through this research, we seek to bridge the gap between ophthalmic research and physical education, providing insights into how visual impairments like myopia can impact an adolescent's ability to engage in physical activities. The implications of this study are far-reaching, potentially guiding interventions that can improve the visual health of adolescents and, in turn, encourage their participation in physical fitness and games, which are integral to their holistic development. (Park, Ko, Park, Kim, & Choi, 2022; Tan et al., 2022).

2. Literature review

2.1 Introduction to Myopia

Myopia results from a mismatch between the axial length of the eye and the power of its refractive components that causes images to be focused in front of the retina and blurred vision at distance (Carr & Stell, 2017).. Environmental factors that influence myopia onset include near work and less outdoor activities. Evidences show that there are relationship between myopia prevention and bright light exposure outdoors (Read, Collins, & Vincent, 2015; Wang et al., 2021).

The optical coherence tomography (OCT) angiography may aid the detection or diagnose of Myopia (Ang et al, 2018). Advances in ocular imaging devices, such as OCT, have enabled the visualization of pathologic changes because of myopia. The microscopic changes in both the posterior segment (choroid, retina, sclera, and the optic nerve) and the anterior segment can be observed. According to Kim & Cho and Wang et al (Kim & Cho, 2015; Wang et al., 2021), the mammalian models show that during the myopia development, scleral thinning and tissue loss occur.

Decreased collagen fiber diameter and collagen crosslinking (CXL) and reduced dry weight and hydroxyproline content are seen in the mammalian models. (Cho, Kim, & Yang, 2009) argues that the dominant eye and the non-dominant eye may show different performance in refractive power and vision when examining a target object at the same time. As a result, myopia is more progressed in the dominant eye than the non-dominant eye.

2.2 3D Image Reconstruction

Optical Coherence Tomography (OCT) systems can image the anterior segment as well as the posterior segment of the eye such as the retina, BM, RPE, and choroid (Hoang, Chua, Ang, & Schmetterer, 2020). OCT can obtain 2D (Two-dimensional) or 3D (three-dimensional) retinal tomography images with micron resolution on living tissue. OCT has been widely used in the study of various fundus lesions in recent years because it can objectively and quantitatively measure and analyze retinal and choroid thickness. More importantly, it is non-invasive, non-invasive, accurate and reproducible. The fundus images obtained by OCT scanning can be preprocessed to extract the contours of retina and choroid, and the interpolation function of Matlab is used to reconstruct multiple OCT images into 3D fundus images, making the fundus layer structure more intuitive.

At the same time, the thickness, volume and other parameters of fundus layer can be calculated on the basis of 3D reconstruction by using Matlab calculation function. providing better observation of the occurrence and

development of the Myopia. (Dubis, McAllister, & Carroll, 2009) present an approach to 3D Image Reconstruction of the retinal volume. It is conducted with Custom Matlab programs. a 3D map of the fovea is produced by using the surf function, combined with the thesix B-scans from a fast mac data set.

The shifted raw data sets are fitted to a 2D (two dimentional) DoG function. These fits provide a qualitative picture of the fovea. MatLab code is used for creating 3D renderings from .txt formatted thickness values.

2.3 Similarity Measurement Method of Fuzzy Variables

This paper is based on the k-NN padding algorithm, and expands its scope of application to fuzzy situations. Since we need to find the k most "similar" examples with missing fuzzy information examples, we need to use the similarity measure between fuzzy variables.

The tools commonly used to measure the similarity between two fuzzy variables are closeness and distance, where closeness represents the similarity of two fuzzy variables, and distance represents the difference between the two fuzzy variables. They represent two aspects of the same thing, with opposite meanings, but generally speaking, the sum of the two is 1. The following introduces several common fuzzy variables closeness and distance:

(1) Maximum-minimum closeness: Assuming that ξ, η are two fuzzy variables with discrete values of $(x_1, x_2, \ldots x_n)$, and their probability distributions are $\mu_\xi(x)$ and $\mu_\eta(x)$ respectively, then the maximum-minimum posting progress between ξ, and η is as shown in (1):

$$N_m(\xi,\eta) = \frac{\sum_{i=1}^{n}(\mu_\xi(x_i) \wedge \mu_\eta(x_i))}{\sum_{i=1}^{n}(\mu_\xi(x_i) \vee \mu_\eta(x_i))} \quad (1)$$

When ξ, η are continuous fuzzy variables on the interval [a, b], the maximum-minimum posting progress between ξ, η is shown in (2):

$$N_m(\xi,\eta) = \frac{\int_a^b (\mu_\xi \cap \mu_\eta)(x)dx}{\int_a^b (\mu_\xi \cup \mu_\eta)(x)dx} \quad (2)$$

Similarly, there is the minimum average closeness. The minimum average closeness of the discrete case is shown in (3):

$$N_A(\xi,\eta)=\frac{\sum_{i=1}^{n}(\mu_\xi(x_i)\wedge\mu_\eta(x_i))}{\sum_{i=1}^{n}\frac{1}{2}(\mu_\xi(x_i)+\mu_\eta(x_i))} \quad (3)$$

The minimum average closeness of the continuous case is:

$$N_A(\xi,\eta)=\frac{\int_a^b(\mu_\xi\cap\mu_\eta)(x)dx}{\frac{1}{2}\int_a^b(\mu_\xi(x)+\mu_\eta(x))dx} \quad (4)$$

Assuming that ξ, η are two fuzzy variables with discrete values of $(x_1,x_2,\ldots x_n)$, and their probability distributions are $\mu_\xi(x)$ and $\mu_\eta(x)$ respectively, then the the Minkowski distance is defined as (5):

$$d(\xi,n)=\left(\frac{\sum_{i=1}^{n}|\mu_\xi(x_i)-\mu_\eta(x_i)|^p}{n}\right)^{\frac{1}{p}},p\geq1 \quad (5)$$

When P =1, the Minkowski distance is the Hamming distance:

$$d_H(\xi,\eta)=\frac{\sum_{i=1}^{n}|\mu_\xi(x_i)-\mu_\eta(x_i)|}{n} \quad (6)$$

When P = 2, the Minkowski distance is the Euclidean distance:

$$d_E(\xi,\eta)=\left(\frac{\sum_{i=1}^{n}|\mu_\xi(x_i)-\mu_\eta(x_i)|^2}{n}\right)^{\frac{1}{2}} \quad (7)$$

Next, use the gradient average integral to represent the distance: Assuming that ξ,η are two fuzzy variables, the distance between them is defined as:

$$d_p(\xi,\eta)=|p(\xi)-p(\eta)| \quad (8)$$

When ξ, η are triangular and trapezoidal fuzzy variables, they are calculated as follows:

$$P(\xi)=\frac{a_1+4a_2+a_3}{6} \quad (9)$$

$$P(\eta)=\frac{b_1+4b_2+b_3}{6} \quad (10)$$

$$P(\xi)=\frac{a_1+2a_2+2a_3+a_4}{6} \quad (11)$$

$$P(\eta)=\frac{b_1+2b_2+2b_3+b_4}{6} \quad (12)$$

In summary, we have completed the research on the fuzzy data filling algorithm, and then we will start the experiment.

3. Materials and Methods

3.1. Study Population

The research subjects were 59 patients with myopic an isometropia selected from the optometry center of a certain hospital in a city during the period of August 2020 to August 2021, with age arranging from 8 to 18 years.

3.2 Data Acquisition

Experiment of Each Element of the Refractive Three-Dimensional Image Structure of Myopic eyes of Adolescents Based on Artificial Intelligence Electronic Health

3.3 3D Image Structure Platform Construction

In the design of 3D perception and information reconstruction system based on active vision, the effective projection of the light source plays a vital role in the structure and accuracy of the point cloud data. In order to adapt to the function of ODVS that can shoot 360-degree panoramic images of the scene at the same time, the mobile surface laser generator must project a laser light source that can cover 360 degrees in the horizontal direction of the scene.

It can move up and down in the vertical direction to complete the scan of the scene. Based on this design goal, the following article will first introduce the principle of laser ranging, and then explain the specific design of the moving surface laser generator in ASODVS and the assembly method of the moving surface laser light source. Commonly used laser ranging principles are: triangle ranging method, time-of-flight method and phase method. The triangulation

method uses spatial geometric relationships to calculate the distance from the scan center to the target point, thereby completing the calculation of spatial 3D information.

The laser scanning system using this method is mainly composed of a laser generator and a CCD camera, which form a spatial plane triangle with the target point, as shown in Figure 1. The emitted light, incident light and baseline all come from the scanner angle sensor. Its included angle can complete geometric calculations to obtain 3D information.

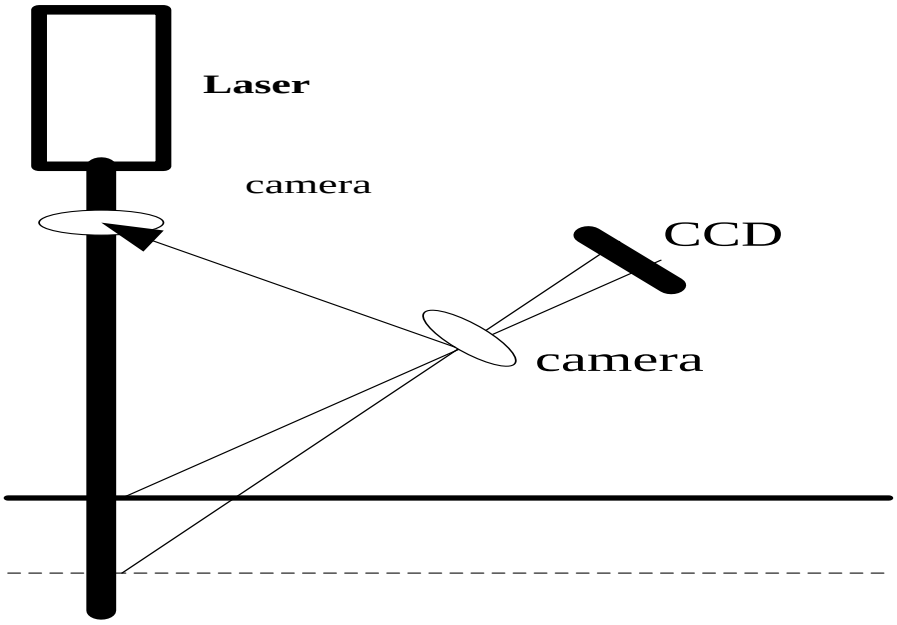

Figure 1: Triangular Ranging Method

The time-of-flight method and phase ranging method, as the distance measurement principle, the transmitting and receiving devices of the laser rangefinder must be laser receivers and transmitters, which belong to point-to-point measurement; while the receiver of the triangulation method is a CCD imaging chip. The CCD imaging chip can obtain planar image information, so that the laser of the triangulation method can use a line laser light source or a surface laser light source. This method not only improves the scanning efficiency of the laser, but also effectively reduces the complexity of the system.

If the aperture produced by the projection of the moving surface laser generator in the panoramic sequence image is a series of perfect circles centered on the panoramic image, it means that the ASODVS configuration is over; otherwise, fine-tuning is required to make the ASODVS meet the ideal design requirements. In addition to the observation method, you can also save the panoramic image with laser information generated in the above process, and use the algorithm to analyze the image to determine whether the ASODVS has reached the assembly requirements. Figure 2 is the flow chart of the entire

system:

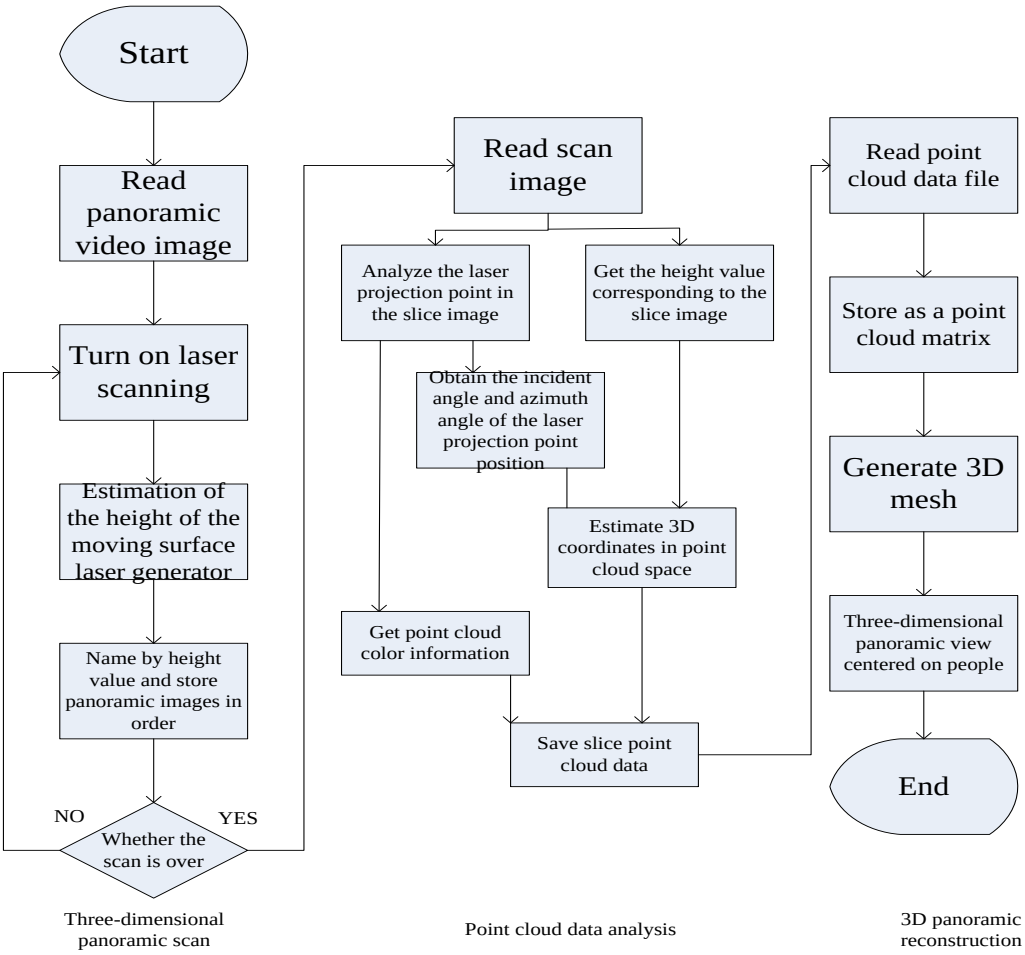

Figure 2: System Flow Chart

When SODVS calculates the three-dimensional coordinates of a space point, it first needs to analyze the laser point in the panoramic image. The analysis algorithm of the laser point includes the algorithm based on the HIS color model, the algorithm based on the inter-frame difference algorithm, and the three-frame difference algorithm. The sampling speed of ASODVS is also closely related. ASODVS inevitably has some errors in the calculation of the three-dimensional coordinates of the space point. The maximum error of the distance from the point cloud to the single viewpoint in the statistical space is within 3%.

3.4 Network Model Configuration

There are two important files for training a network model, one is the configuration file that defines the network structure, and the other is the solver file that sets the training parameters. This section explains the network configuration file adjusted for your own training data. The methods in this chapter are based on the ResNet 101 level. For the network data level (defining network input), this article converts the color image into the lmdb data format

with higher reading performance as the network input. In the experiment, the average value of the image will be subtracted for training and testing, which will improve the speed and accuracy to a certain extent. Calculating the average is to calculate the average of all training samples. Caffe provides the average value of data calculated in lmdb format. Average file value in binary format.

The default input size of ResNet is 224×224, and the image size of the training set in this article is 101×101. Direct training will cause the dimension of the feature map to be reduced to 1 before reaching the fully connected layer, and the subsequent convolution cannot be performed. The operation results in the training failure. You can perform zero padding on the input image to expand the size to 224×224. This article chooses to modify the size of the convolution step in one of the residual blocks, so that the feature map has a different dimension after passing through this residual block. In this way, the network can adapt to the input of 101×101 size, which can be seen in the ResNet framework table listed above.

3.5 Objects and Experimental Preparation

Research topics are selected from: From August 2018 to August 2019, 59 patients with myopia acuity were collected from outpatient clinics of optometry centers in specific hospitals in specific cities. The age of the patient is 8 to 18 years old, and the standard of anisotropy is: the difference of binoculars ⩾ 1.50D or the difference of astigmatism ⩾ 1.00D. Through systematic examination and consultation of the eyes, patients with the following eye diseases and medical history were excluded: strabismus, amblyopia, congenital eye diseases, organic eye diseases, nystagmus, etc., as well as patients suffering from eye or eye trauma.

Among them, 30 were males and 29 were females, aged 8 to 35 years old, with an average age of 21.0±7.4 years. Adolescent group: 27 people from 8 to 18 years old; Adult group: 32 people from 19 to 35 years old. It is divided into 26 cases of low eyeball power (Eyeball equivalent spherical power difference<2.50D) and 33 cases of high eyeball power (Eyeball equivalent spherical power difference⩾2.50D). Equipment used in eye examinations: point light source lighting, TOPCON SL-1E slit, NEITZ PUS-1 ophthalmoscope, NIDEK SSC-330 projection map. In general eye examinations, the Hirschberg test corneal reflex method, the cap test and the cap-to-cap test rule out obvious strabismus.

Use a slit lamp microscope and direct ophthalmoscope to rule out other organic eye diseases. International standard visual acuity chart examination, binocular corrected visual acuity> 0.8, excluding amblyopia. In the selection of research equipment, we choose handheld light source, wireless retinoscope, computerized KIA-8700 refractometer, NETFIX automatic refractory core,

TOPOE HD-9 rangefinder.

4. Various Elements of the Structure of the Refractive Three-Dimensional Image of Adolescents with Myopia Based on Artificial Intelligence and Electronic Health

4.1 Data Set of Each Element of Three-Dimensional Image Structure

From the UCI machine learning data set, 12 commonly used classification benchmark data sets were selected for deletion and fuzzification, and then the experiment was carried out. The specific description of the data set is shown in Table 1.

Table 1: 12 Classification UCI Data Set Description

NUMBER	DATA SET	NUMBER OF EXAMPLES	NUMBER OF ATTRIBUTES	NUMBER OF CATEGORIES
1	Arrhythmia	455	279	16
2	Blood	748	5	2
3	BreastDv	569	32	2
4	BreastP	198	34	2
5	Credit	690	15	2
6	Ecoli	336	8	6
7	Glass	214	10	7
8	Haberman	306	3	2
9	Hepatitis	155	19	2
10	Spambase	4601	57	2
11	Teaching	152	5	3
12	Wine	178	13	3

In order to fully verify the effect of each algorithm, the 12 complete data sets were deleted at the proportions of 10%, 20%, 30%, and 40% respectively, that is, the data of a rated proportion was randomly selected and deleted to make them an incomplete data set. Fuzzy the conditional attribute parts of the incomplete clear data respectively to generate 12 triangular incomplete fuzzy sets and 12 trapezoidal incomplete fuzzy sets. The following will compare the five common distances, namely the maximum-minimum closeness, lattice closeness, Euclidean distance, gradient average integral representing distance, and the distance of intuitionistic fuzzy concentration, and compare them with the distance metric we proposed.

For the convenience of description, they are marked as d1, d2, d3, d4, d5, and d6 in order. All experiments are performed on 24 incomplete fuzzy data sets with different missing ratios, that is, the missing rates are 10% and 20%, respectively., 30% and 40% of triangular and trapezoidal incomplete fuzzy data sets. Because the fuzzy data k-NN filling algorithm is used, the value of k is

fixed to the same value, and k=10 is used here. As follows: The comparison of different distance measures in the fuzzy data k-NN filling algorithm (triangular data set, missing rate 10%) is shown in Table 2:

Table 2: Comparison of Different Distance Measures in Fuzzy Data k-NN Filling Algorithm （10%）

DATA SET	D1	D2	D3	D4	D5	D6
1	0.0751	0.1524	0.0797	0.1365	0.0798	0.0749
2	0.0710	0.1123	0.0751	0.0958	0.0785	0.0706
3	0.0740	0.1165	0.0811	0.1019	0.0803	0.0753
4	0.1039	0.1089	0.1042	0.1246	0.1051	0.1013
5	0.1222	0.1416	0.1156	0.1482	0.1323	0.1216
6	0.0572	0.1205	0.0609	0.1236	0.0609	0.0560
7	0.0826	0.1236	0.0837	0.1395	0.0831	0.0837
8	0.0698	0.1213	0.0782	0.2036	0.0809	0.0708
9	0.0889	0.1203	0.0878	0.1102	0.0905	0.0840
10	0.1778	0.1797	0.1756	0.2006	0.1806	0.1791
11	0.0631	0.0803	0.0625	0.0745	0.0652	0.0607
12	0.1295	0.1652	0.1311	0.1456	0.1325	0.1303

The comparison of different distance measures in the fuzzy data k-NN filling algorithm (triangular data set, missing rate 20%) is shown in Table 3:

Table 3: Comparison of Different Distance Measures in Fuzzy Data k-NN Filling Algorithm （20%）

DATA SET	D1	D2	D3	D4	D5	D6
1	0.1005	0.1219	0.1068	0.1552	0.1103	0.1016
2	0.01284	0.1586	0.1295	0.1889	0.1282	0.1270
3	0.1080	0.1216	0.1102	0.1092	0.1096	0.1047
4	0.1254	0.1516	0.1120	0.2115	0.1245	0.1242
5	0.0712	0.0756	0.0701	0.0856	0.0721	0.0708
6	0.0682	0.1320	0.0699	0.1122	0.0712	0.0709
7	0.0999	0.1366	0.1020	0.1422	0.1006	0.0997
8	0.1031	0.1130	0.1066	0.1125	0.1056	0.1048
9	0.0989	0.1362	0.1102	0.1298	0.1200	0.1004
10	0.1980	0.2008	0.1989	0.2003	0.1991	0.1975
11	0.762	0.0853	0.0783	0.0957	0.0821	0.0753
12	0.1428	0.1524	0.1456	0.1652	0.1468	0.1419

The comparison of different distance measures in the fuzzy data k-NN

filling algorithm (triangular data set, missing rate 30%) is shown in Table 4:

Table 4: Comparison of Different Distance Measures in Fuzzy Data k-NN Filling Algorithm （30%）

DATA SET	D1	D2	D3	D4	D5	D6
1	0.1206	0.1369	0.1225	0.1265	0.1226	0.1200
2	0.1498	0.2003	0.1495	0.1603	0.1520	0.1508
3	0.1270	0.1302	0.1293	0.1335	0.1285	0.1265
4	0.1602	0.2008	0.1623	0.2115	0.1633	0.01632
5	0.0916	0.1252	0.1216	0.1323	0.1015	0.0930
6	0.0885	0.1230	0.0902	0.1003.	0.0895	0.0871
7	0.1125	0.1365	0.1128	0.1422	0.1154	0.1132
8	0.1335	0.1356	0.1338	0.1385	0.1345	0.1328
9	0.1096	0.1354	0.1059	0.1298	0.1089	0.1124
10	0.1825	0.1953	0.1893	0.2226	0.1853	0.1881
11	0.0952	0.1125	0.0958	0.1252	0.0962	0.0921
12	0.1920	0.2324	0.1926	0.2190	0.1930	0.1901

After collecting the above data, the average error of drawing the triangle data set is shown in Figure 3;

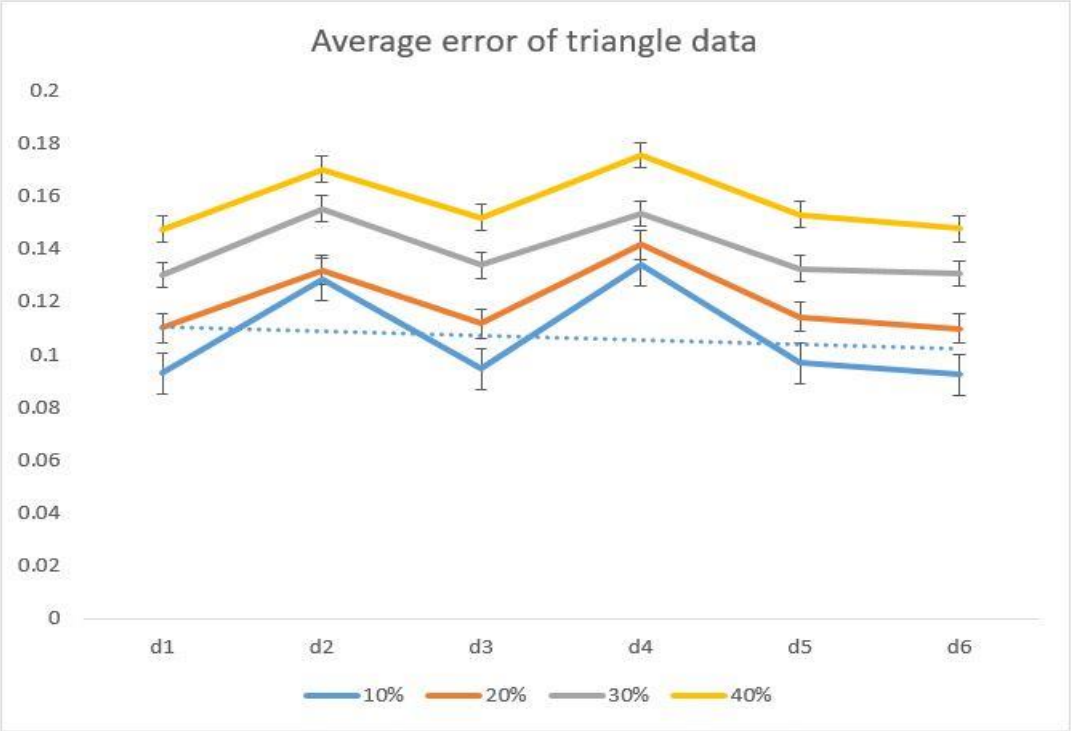

Figure 3: Average Error of Triangle Data

The average error on the trapezoidal data is shown in Figure 4:

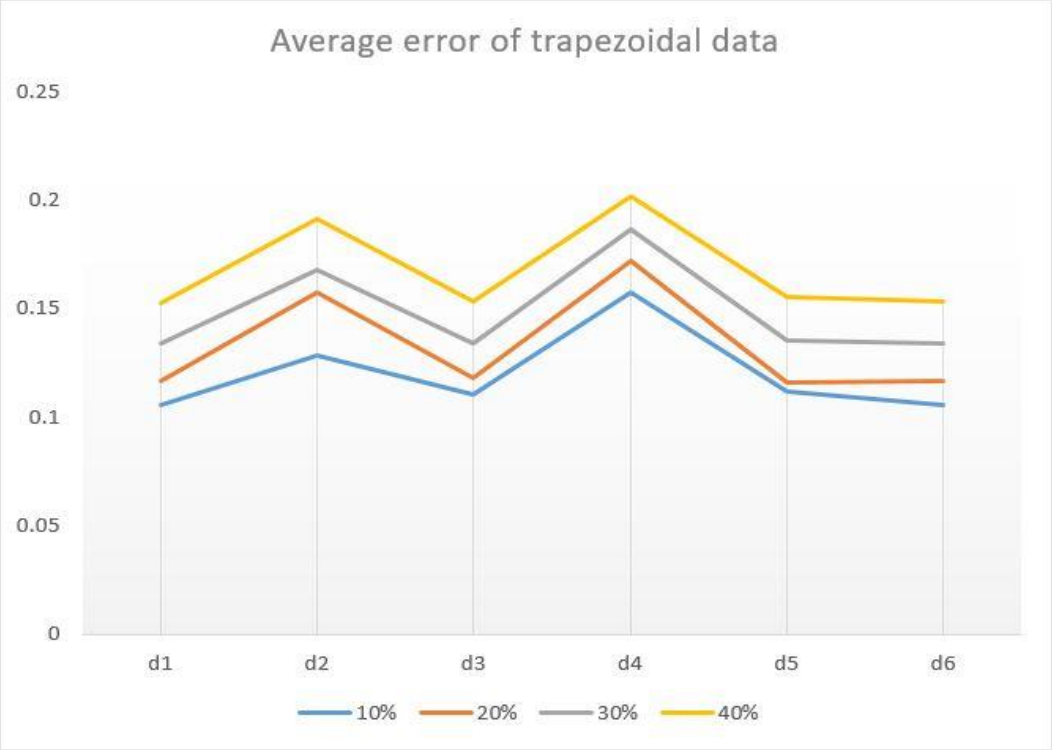

Figure 4： Average Error of Trapezoidal Data

Analyzing the content of the chart, it can be seen that all filling methods show a trend that the higher the missing rate and the greater the filling error, that is, the lower the filling accuracy; among the six metrics, d1, d3, d5, and d6 have better effects, and the error is filled.

Significantly smaller than the other two metrics; among the four better-performing metrics, d6 has the best effect, which shows the effectiveness of the newly proposed distance metric; d1, d5, and d6 are all distance metrics considering the area, and the effect is better than that The other three are better, which shows that this type of distance defined based on area is more suitable for searching for similar examples for filling research.

4.2 Experimental Analysis of Adolescent Refractive

In the research of this article, the subjects are divided into two groups according to the difference of the equivalent spherical mirrors of the two eyes. In the low-power parallax method patient group, there are 26 cases (two eyeball lens equivalent difference <2.50D) and 15 males have 30 eyes.

They accounted for 57.7%, and 22 eyes of 11 women, accounting for 42.3%. There were 33 cases in the patient group with high visual illusion (two-eye equivalent spherical aberration $\geqslant$ 2.50D). Males have 15 eyes and 30 eyes, accounting for 45.5%, There were 18 females and 36 females, accounting for 54.5%. As shown in Table 5:

Table 5: Basic Situation of Each Group

GROUPING	NUMBER	SEXUAL(M/F)
Low anisometropia	26	15/11
high anisometropia	33	15/18
account	59	30/29

The average adjustment range of the dominant eye in the low isometric eyeshadow group is 12.22±3.92D, and the average adjustment range of the non-dominant eye is 12.35 ± 3.79D. The difference was not statistically significant (t=-0.30, P>0.05); the high-level contour vision group was the main one. The average adjustment range of eyes was 11.60 ± 2.26D, and the average adjustment range of non-dominant eyes was 11.98 ± 2.58D, the difference was not statistically significant (t=-1.30, P>0,05). See Table 6:

Table 6: Comparison of Accommodation Range between Dominant Eye and Non-Dominant Eye

	DOMINANT EYE ACCOMMODATION	NON-DOMINANT EYE ACCOMMODATION AMPLITUDE	T	P
Low anisometropia	12.22±3.92	12.35±3.79	-0.3	0.77
high anisometropia	11.60±2.26	11.98±2.58	-1.3	0.2

4.3 Comparison of Myopia Function in Patients with Different Degrees of Binocular Vision

Comparing the functions of the two groups of patients with different degrees of myopia, in the low-quality IOP measurement group, there were 9 abnormal cases, accounting for 34.62%, and 17 normal cases, accounting for 65.38%. In the high anisotropy group, 20 cases were abnormal, accounting for 60.62%, and 13 cases were normal, accounting for 39.39%. According to the chi-square test of the four-point table, the group with high anisotropy had a higher incidence of abnormal surgery near vision, and the difference was statistically significant. As shown in Table 7:

Table 7: Comparison of Near Vision Function in Different Degree Groups

GROUPING	NUMBER	NORMAL	ABNORMAL
Low anisometropia	26	17(65.38%)	9(34.62)
high anisometropia	33	13(39.39%)	20(60.61%)
amount	59	30(50.85%)	29(49.15%)

According to the statistical results of the SPSS software, in the low-level isokinetic imaging group, 21 cases had normal stereo sound, accounting for 80.77%, 5 cases were abnormal (≥60"), accounting for 19.23%, and the

stereotype was 71.92± 73.92". In the high anisotropy group, 18 cases had normal steric acidity, accounting for 54.55%, and 15 cases had abnormal acidity, accounting for 45.45%. The average three-dimensional acidity is 130.91± 119.83". The average three-dimensional acidity ratio of the high isotacticity group is lower. The grade group is worse, but the difference is not statistically significant (z = -1.70, P>The four-point square table is shown in Table 8, The stereo abnormality rate of the high-contour stereoscopic measurement group was higher than that of the low-contour stereoscopic measurement group, and the difference was statistically significant. As shown in Table 8:

Table 8：Stereoscopic Comparison of Different Groups

GROUPING	NUMBER	NORMAL	ABNORMAL
Low anisometropia	26	21(80.77%)	5(19.23%)
high anisometropia	33	18(39.39%)	15(60.61%)
amount	59	30(50.85%)	23(49.15%)

5. Conclusions

The study's application of deep learning techniques in analyzing 3D Optical Coherence Tomography Images has provided valuable insights into the refractive characteristics of adolescent myopia. Our findings reveal significant variations in stereo vision among adolescents, which have substantial implications for their engagement in physical fitness and games. The observed differences in stereo vision, particularly in groups with varying levels of anisotropy, underscore the impact that visual clarity and depth perception can have on an adolescent's ability to participate in physical activities.

The correlation between abnormal stereo vision and decreased participation in physical fitness and games highlights a critical area of concern. Adolescents with impaired stereo vision, as indicated by the higher rates of abnormalities in certain groups, may face challenges in activities that require depth perception and fine motor coordination, potentially leading to reduced physical activity and its associated health benefits.

These findings emphasize the importance of early detection and intervention for myopia and refractive issues in adolescents. By addressing these visual impairments, there is potential to not only improve their visual health but also enhance their engagement in physical activities and games. This is crucial for their overall development, as regular participation in physical activities is known to benefit mental and physical health, social skills, and academic performance. In conclusion, this research highlights the need for continued exploration of the relationship between adolescent myopia, 3D visual structure, and physical activity. Understanding and mitigating the impacts of visual impairments on adolescents' participation in fitness and games can contribute significantly to their holistic health and well-being.

REFERENCES

Abdalla, T. M., Elawamry, A. I., Nada, O. T., & Helal, M. R. (2020). A comparative study of OCT findings in low and high myopia. *Journal of the Egyptian Ophthalmological Society, 113*(1), 22.

Ang, M., Wong, C. W., Hoang, Q. V., Cheung, G. C. M., Lee, S. Y., Chia, A., . . . Schmetterer, L. (2019). Imaging in myopia: potential biomarkers, current challenges and future developments. *British Journal of Ophthalmology, 103*(6), 855-862.

Asmar, R., Benetos, A., Topouchian, J., Laurent, P., Pannier, B., Brisac, A.-M., . . . Levy, B. I. (1995). Assessment of arterial distensibility by automatic pulse wave velocity measurement: validation and clinical application studies. *Hypertension, 26*(3), 485-490.

Carr, B. J., & Stell, W. K. (2017). The science behind myopia. *Webvision: The Organization of the Retina and Visual System [Internet]*.

Cho, K.-J., Kim, S.-Y., & Yang, S.-W. (2009). The refractive errors of dominant and non-dominant eyes. *Journal of the Korean Ophthalmological Society, 50*(2), 275-279.

Dubis, A. M., McAllister, J. T., & Carroll, J. (2009). Reconstructing foveal pit morphology from optical coherence tomography imaging. *British Journal of Ophthalmology, 93*(9), 1223-1227.

Esteva, A., Chou, K., Yeung, S., Naik, N., Madani, A., Mottaghi, A., . . . Socher, R. (2021). Deep learning-enabled medical computer vision. *NPJ digital medicine, 4*(1), 5.

Hoang, Q. V., Chua, J., Ang, M., & Schmetterer, L. (2020). Imaging in myopia. *Updates on Myopia: A Clinical Perspective*, 219-239.

Huang, H.-M., Chang, D. S.-T., & Wu, P.-C. (2015). The association between near work activities and myopia in children—a systematic review and meta-analysis. *PloS one, 10*(10), e0140419.

Karsai, I., Montano, E., & Schmickl, T. (2016). Bottom-up ecology. *Letters in Biomathematics, 3*(1), 161–180-161–180. doi:https://doi.org/10.30707/LiB3.1Karsai

Kim, H. K., & Cho, K. J. (2015). The angle kappa in dominant and non-dominant eye. *Journal of the Korean Ophthalmological Society, 56*(4), 494-498.

Lanca, C., Yam, J. C., Jiang, W. J., Tham, Y. C., Hassan Emamian, M., Tan, C. S., . . . Zhu, D. (2022). Near work, screen time, outdoor time and myopia in schoolchildren in the Sunflower Myopia AEEC Consortium. *Acta ophthalmologica, 100*(3), 302-311.

Li, S.-M., Li, S.-Y., Kang, M.-T., Zhou, Y., Liu, L.-R., Li, H., . . . Mitchell, P. (2015). Near work related parameters and myopia in Chinese children: the Anyang Childhood Eye Study. *PloS one, 10*(8), e0134514.

Lu, L., Zhou, E., Yu, W., Chen, B., Ren, P., Lu, Q., . . . Tang, X. (2021). Development of deep learning-based detecting systems for pathologic myopia using retinal fundus images. *Communications biology, 4*(1), 1225.

Megreli, J., Barak, A., Bez, M., Bez, D., & Levine, H. (2020). Association of Myopia with cognitive function among one million adolescents. *BMC public health, 20*(1), 1-9.

Muralidharan, A. R., Lança, C., Biswas, S., Barathi, V. A., Wan Yu Shermaine, L., Seang-Mei, S., . . . Najjar, R. P. (2021). Light and myopia: from epidemiological studies to neurobiological mechanisms. *Therapeutic advances in ophthalmology, 13*, 25158414211059246.

Park, S.-J., Ko, T., Park, C.-K., Kim, Y.-C., & Choi, I.-Y. (2022). Deep learning model based on 3D optical coherence tomography images for the automated detection of pathologic myopia. *Diagnostics, 12*(3), 742.

Pitts, P. (2020). The spreading cancer of counterfeit drugs. *Journal of Commercial Biotechnology, 25*(3), 20-14.

Read, S. A., Collins, M. J., & Vincent, S. J. (2015). Light exposure and eye growth in childhood. *Investigative Ophthalmology & Visual Science, 56*(11), 6779-6787.

Tan, Y., Zhu, W., Zou, Y., Zhang, B., Yu, Y., Li, W., . . . Liu, Z. (2022). Hotspots and trends in ophthalmology in recent 5 years: Bibliometric analysis in 2017–2021. *Frontiers in Medicine, 9*.

Todorov, T., Mitrev, R., & Penev, I. (2020). Force analysis and kinematic optimization of a fluid valve driven by shape memory alloys. *Reports in Mechanical Engineering, 1*(1), 61-76.

Townsend, K. A., Wollstein, G., & Schuman, J. S. (2008). Clinical application of MRI in ophthalmology. *NMR in Biomedicine: An International Journal Devoted to the Development and Application of Magnetic Resonance In vivo, 21*(9), 997-1002.

Wang, W.-Y., Chen, C., Chang, J., Chien, L., Shih, Y.-F., Lin, L. L., . . . Wang, I.-J. (2021). Pharmacotherapeutic candidates for myopia: A review. *Biomedicine & Pharmacotherapy, 133*, 111092.